

# PHOTONICS Research

## Tunable waveguide mode of hyperbolic phonon polaritons in $\alpha$ -MoO<sub>3</sub> flake/gold slit composite structure

NAN DENG,<sup>1,†</sup> ZHONGAO HUANG,<sup>1,†</sup> KAI WANG,<sup>1,2,\*</sup> KUN WANG,<sup>1</sup> XIAOBO HAN,<sup>3</sup> XINYING ZHANG,<sup>1</sup> BING WANG,<sup>1</sup> HUA LONG,<sup>1,4</sup> AND PEIXIANG LU<sup>1,3</sup>

<sup>1</sup>Wuhan National Laboratory for Optoelectronics and School of Physics, Huazhong University of Science and Technology, Wuhan 430074, China

<sup>2</sup>School of Electronic and Information Engineering, Hubei University of Science and Technology, Xianning 437100, China

<sup>3</sup>Hubei Key Laboratory of Optical Information and Pattern Recognition, Wuhan Institute of Technology, Wuhan 430205, China

<sup>4</sup>e-mail: longhua@hust.edu.cn

<sup>†</sup>These authors contributed equally to this work.

\*Corresponding author: kale\_wong@hust.edu.cn

Received 17 May 2024; revised 13 September 2024; accepted 26 September 2024; posted 27 September 2024 (Doc. ID 530540); published 2 December 2024

Hyperbolic phonon polaritons (HPhPs) in van der Waals layered polar crystals exhibit extreme light confinement capability, providing an unprecedented research opportunity to manipulate nanoscale midinfrared photons. Precise tuning of HPhPs propagation characteristics and near-field energy routing is crucial for applying polaritonic devices. Here, we demonstrate a widely tunable waveguide mode of HPhPs in an  $\alpha$ -MoO<sub>3</sub> flake/gold slit composite structure. By varying the width of the gold slit from 3  $\mu$ m to 220 nm, the compression ratio of HPhPs wavelength relative to the incident light wavelength can be adjusted from 35% to 8.6%, respectively. This is attributed to the introduction of the gold slit, which can effectively excite and guide HPhPs within an  $\alpha$ -MoO<sub>3</sub> flake, forming a confined waveguide mode. Notably, the excitation efficiency of HPhPs in the nanoscale ultranarrow waveguide can be enhanced by integrating an extended port at the waveguide port. In addition, the routing of polaritons in a Y-shaped waveguide is realized by modulating the frequency of the incident light. This work presents a promising platform for manipulating deep subwavelength polaritons in planar photonic devices for infrared applications. © 2024 Chinese Laser Press

<https://doi.org/10.1364/PRJ.530540>

### 1. INTRODUCTION

Hyperbolic phonon polaritons (HPhPs), a type of quasiparticle resulting from the coupling between electromagnetic waves and collective lattice vibrations in hyperbolic polar materials, enable ultraconfined, ultralow optical losses, and highly directional wave propagation at the nanoscale. In recent studies, a range of van der Waals crystals have been experimentally shown to support HPhPs, including hexagonal boron nitride (hBN) [1,2], orthorhombic-phase molybdenum trioxide ( $\alpha$ -MoO<sub>3</sub>) [3–5], and vanadium pentoxide ( $\alpha$ -V<sub>2</sub>O<sub>5</sub>) [6]. The former is characterized by uniaxial hyperbolicity, resulting in isotropic dielectric response within the plane [7,8]. The latter two are biaxial crystals, where the polariton propagation strictly occurs along the in-plane hyperbolic directions, with more innovative in-plane hyperbolic forms reported in crystals with lower symmetry, such as hyperbolic shear polaritons in monoclinic crystals [9,10]. These polaritons support high wave confinement due to their large momenta [2,11], resulting in enhanced interactions between light and matter [12,13]. Recently, new

mechanisms are proposed to achieve the tunable HPhPs through  $\alpha$ -MoO<sub>3</sub> flake, such as intrinsic chirality [14], gate-tuning hybrid polaritons [15], and spin Hall effect [16]. This enables precise control over energy flow [17], facilitating various applications, including infrared sensing [18,19], optical isolation [20], and photodetection [21].

The further progression of polaritons investigation relies heavily on the accurate adjustment of these nanoscale light-matter modes, such as confinement [22–26], propagation [27–30], and dispersion [31–34]. The utilization of polaritonic modes in these van der Waals materials exhibits a combination of tunability, low losses, and ultrahigh confinement, making them exceptionally appealing for the design of nanophotonic devices. Recently, several notable studies have achieved multi-dimensional control of polaritons, such as gate-tunable negative refraction in graphene/ $\alpha$ -MoO<sub>3</sub> heterostructure [35], ultrafast anisotropic dynamics on calcite surfaces [36], and manipulation of higher-order HPhPs on a 3C-SiC nanowire/ $\alpha$ -MoO<sub>3</sub> heterostructure [37]. At the same time, substrate engineering

also makes a significant contribution to manipulating polaritons. Initially, Duan *et al.* discovered that the wavelength of polaritons is sensitive to the dielectric environment [38]. Subsequently, various substrate engineering techniques were realized, such as focusing [39], utilizing phase change material for polariton wavefront engineering [40,41], and using an etched prism for obtaining in-plane anisotropic bending-free refraction [42]. Although it is feasible to control polariton wavelength by changing the dielectric environment or substrate engineering, manipulating polaritons between the dispersions of van der Waals crystal on two different substrates remains an unresolved issue. On the other hand, studies have shown that the HPhPs wavelength in  $\alpha$ -MoO<sub>3</sub> flake on the gold substrate exhibits a significantly high compression ratio relative to the incident light wavelength [43], while the HPhPs have a low compression ratio and ultralow optical losses in suspended  $\alpha$ -MoO<sub>3</sub> flake [44,45]. This inspires us to achieve tuning HPhPs in  $\alpha$ -MoO<sub>3</sub> flakes across a broad spectrum by manipulating the width of the gold slit on the substrate.

Here, we propose and experimentally demonstrate a midinfrared tunable confined waveguide mode by constructing a composite structure consisting of an  $\alpha$ -MoO<sub>3</sub> flake that fully covers the gold slits. The optical near-field response of HPhPs in  $\alpha$ -MoO<sub>3</sub> with different gold slit widths (from 3  $\mu\text{m}$  to 220 nm) is acquired by a photon-induced force microscope (PiFM), realizing the tunability of HPhPs waveguide modes over a wide range. It is found that by integrating an extended port at the nanoscale waveguide port, the excitation efficiency of HPhPs can be significantly improved. This is because when the gold slit width reaches the nanoscale, only a limited quantity of HPhPs can be excited to propagate in the  $\alpha$ -MoO<sub>3</sub> waveguide, and the extended port can increase the quantity of excited HPhPs. In addition, the routing of HPhPs in the Y-shape waveguide is realized by exploiting the characteristic orthogonal transmission of HPhPs in the Reststrahlen band (RB) 1 and RB2 in  $\alpha$ -MoO<sub>3</sub>. Hence, we present an innovative platform of the in-plane polaritonic waveguide, opening up a new avenue for polariton manipulation and offering tremendous potential in infrared sensing, routing, nano-imaging, and on-chip photonics applications.

## 2. THEORY AND DESIGN

$\alpha$ -MoO<sub>3</sub> is a natural hyperbolic material, featuring three mid-infrared RBs (see details in Appendix A). In this work, the detection of the HPhPs waveguide mode in the  $\alpha$ -MoO<sub>3</sub>/gold slit composite structure by PiFM is schematically shown in Fig. 1(a). A pulsed laser (QCL, from Block Engineering) is used to illuminate the gold-coated tip. The polarized tip can excite HPhPs in the  $\alpha$ -MoO<sub>3</sub> flake and form a dipole-dipole force between the tip and  $\alpha$ -MoO<sub>3</sub>, thus enabling the detection of the electromagnetic field distribution at the  $\alpha$ -MoO<sub>3</sub> surface. To maximize the localized force, the laser intensity is modulated at the sideband frequency, which is defined as the difference between the topographic detection frequency of the AFM cantilever and the detection frequency of PiFM. This technique is commonly referred to as sideband modulation mode (see more details in Section 5) [2,46]. By creating different dielectric environments on the substrate, HPhPs excited at the interface will propagate in opposite directions with different wavelengths [Fig. 1(a)].

To figure out the features of the electric field distribution of the HPhPs in the  $\alpha$ -MoO<sub>3</sub> flake/gold slit composite structure, we carry out full-wave numerical simulations. In simulations, we set the width of  $\alpha$ -MoO<sub>3</sub> to 13  $\mu\text{m}$ , the length to 90  $\mu\text{m}$ , the thickness to 242 nm (consistent with the experimental sample), and the groove depth of the gold slit to 1  $\mu\text{m}$ . The width of the gold slit in Fig. 1 is 1.5 and 6  $\mu\text{m}$ , respectively. A dipole is placed on the gold and air substrate interface to excite HPhPs using 2D simulation [Fig. 1(b)]. Due to the gold substrate's extremely high negative permittivity values (on the order of thousands) in the midinfrared range, the gold film can be modeled accurately as a perfect electric conductor (PEC). The fundamental HPhPs mode in suspended  $\alpha$ -MoO<sub>3</sub> is symmetric with respect to the out-of-plane field component,  $E_z$ . The coupling between the HPhPs and the image charges in the metal results in a new type of low-dimensional mode, i.e., the hyperbolic image phonon polariton (HiPP) [11,47]. Due to the forbidden field symmetry, the HiPP in  $\alpha$ -MoO<sub>3</sub> on PEC corresponds to the second-order eigenmode. Compared with the HPhPs in suspended  $\alpha$ -MoO<sub>3</sub>, the HiPP on the metal substrate exhibits much stronger field compression ability.

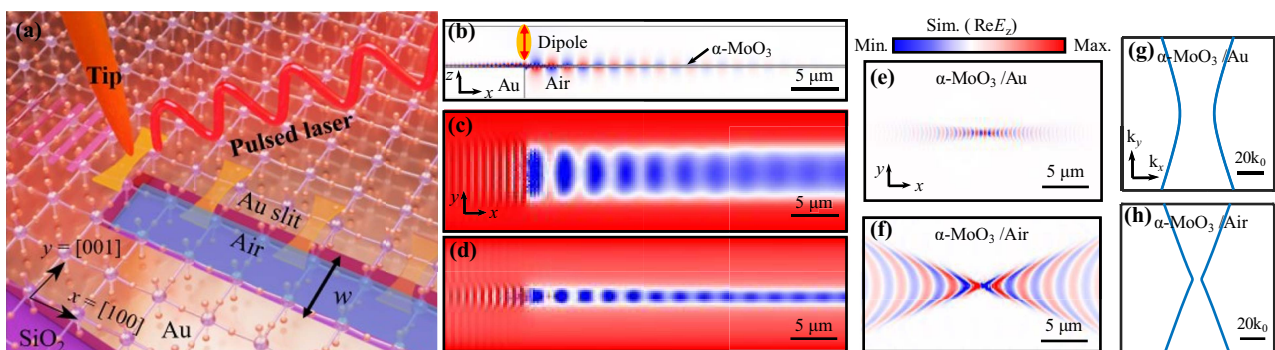


**Fig. 1.** Conceptual design of planar waveguide of HPhPs in  $\alpha$ -MoO<sub>3</sub>. (a) Experimental schematic for launching HPhPs of  $\alpha$ -MoO<sub>3</sub> on gold slit by PiFM setup. (b) Simulation of the 2D near-field distribution of HPhPs in  $\alpha$ -MoO<sub>3</sub> on gold and air substrate, launched by a dipole. (c), (d) 3D simulation; the width of the gold slit is 6  $\mu\text{m}$  in (c) and 1.5  $\mu\text{m}$  in (d). (e), (f) Real-space propagation of HPhPs on gold substrate (e) and air substrate (f) launched by a dipole. (g), (h) IFC of HPhPs in  $\alpha$ -MoO<sub>3</sub> on gold substrate (g) and air substrate (h). The  $\alpha$ -MoO<sub>3</sub> thickness for all simulation settings is 242 nm. The incident light and dipole frequency for all simulation settings is 890  $\text{cm}^{-1}$ .

To investigate the influence of the gold slit width on HPhPs, we conducted 3D simulations of  $\alpha$ -MoO<sub>3</sub> on the gold slits with varying widths. As the loss of HPhPs in the  $y$  direction is so large that it cannot propagate too long in RB1, we choose the frequency in the range of RB2 (e.g., 890 cm<sup>-1</sup>) of  $\alpha$ -MoO<sub>3</sub> as the control band. In Fig. 1(c), it is observed that, when the slit width ( $w$ ) is set to 6  $\mu\text{m}$ , the wavelength of HPhPs in  $\alpha$ -MoO<sub>3</sub> on the gold slit is consistent with that in suspended  $\alpha$ -MoO<sub>3</sub> [Fig. 1(b)]. This finding implies that, at a fixed frequency, as long as the excitation width of  $\alpha$ -MoO<sub>3</sub> is sufficiently large, the wavelength of HPhPs is exclusively determined by the cladding dielectric of  $\alpha$ -MoO<sub>3</sub>. When  $w$  is reduced to 1.5  $\mu\text{m}$  [Fig. 1(d)], the confined waveguide mode of  $\alpha$ -MoO<sub>3</sub> is excited. Since there is a layer of air between  $\alpha$ -MoO<sub>3</sub> and the gold slit, the influence of the SiO<sub>2</sub> substrate as a support on the propagation characteristics of HPhPs can be ignored. At this point, the cladding of  $\alpha$ -MoO<sub>3</sub> remains as air, but it has an obvious compression compared with that of free-standing pure  $\alpha$ -MoO<sub>3</sub> and can be tuned by changing the slit width. This signifies that the wavelength of HPhPs can be precisely adjusted by varying the width of the gold slit. The hyperbolic wavefront propagation of HPhPs on the surface of  $\alpha$ -MoO<sub>3</sub> [Figs. 1(e) and 1(f)], resulting from the pronounced optical anisotropy in the RB2, provides an explanation for the nonrectangular shape of the fringes observed within the slit in Figs. 1(c) and 1(d). The different modes of HPhPs in  $\alpha$ -MoO<sub>3</sub> on gold or air substrate can be described by an isofrequency curve (IFC) at a given incident frequency (more details are presented in Appendix B). The IFCs in Figs. 1(g) and 1(h) show a significant disparity in the wave vectors of HPhPs in  $\alpha$ -MoO<sub>3</sub> on gold and air substrates, implying

the HPhPs waveguide mode can be controlled over a wide range.

### 3. RESULTS AND DISCUSSION

In our experiment, these waveguide composite structures are obtained through the focused ion beam (FIB) etching of slits with varying widths on a gold substrate, followed by mechanical exfoliation from a bulk crystal to obtain high-quality  $\alpha$ -MoO<sub>3</sub> flakes, which are transferred onto the etched substrate (see Section 5). The long axis of the waveguide is along the [100] crystal direction (i.e., the  $x$  axis) of  $\alpha$ -MoO<sub>3</sub> (Fig. 7 in Appendix A), which provides the necessary momentum to excite HPhPs in RB2. Figure 2(a) shows the near-field nano-imaging of the sample by PiFM. The excited HPhPs by the waveguide port are effectively confined within the waveguide composite structure while also enabling the excitation of HPhPs in the  $\alpha$ -MoO<sub>3</sub>/gold substrate through the same port, demonstrating consistent behavior with the prior simulation. Figure 2(b) is the near-field amplitude fringe profiles extracted along the dashed lines shown in Fig. 2(a). It is observed that, due to the additional loss and strong field confinement brought by the gold substrate, the HPhPs on the gold substrate decay quickly, while the HPhPs in the waveguide can propagate over a longer distance. To quantitatively describe the influence of waveguide width on HPhPs, we obtain the momentum-space spectra of the waveguided modes by imposing the fast Fourier transform (FFT) on the near-field fringe profiles [Fig. 2(c)]. With the increase of waveguide width, the main peak position of the FFT exhibits a significant blueshift, which demonstrates that precise manipulation of the HPhPs waveguide mode can

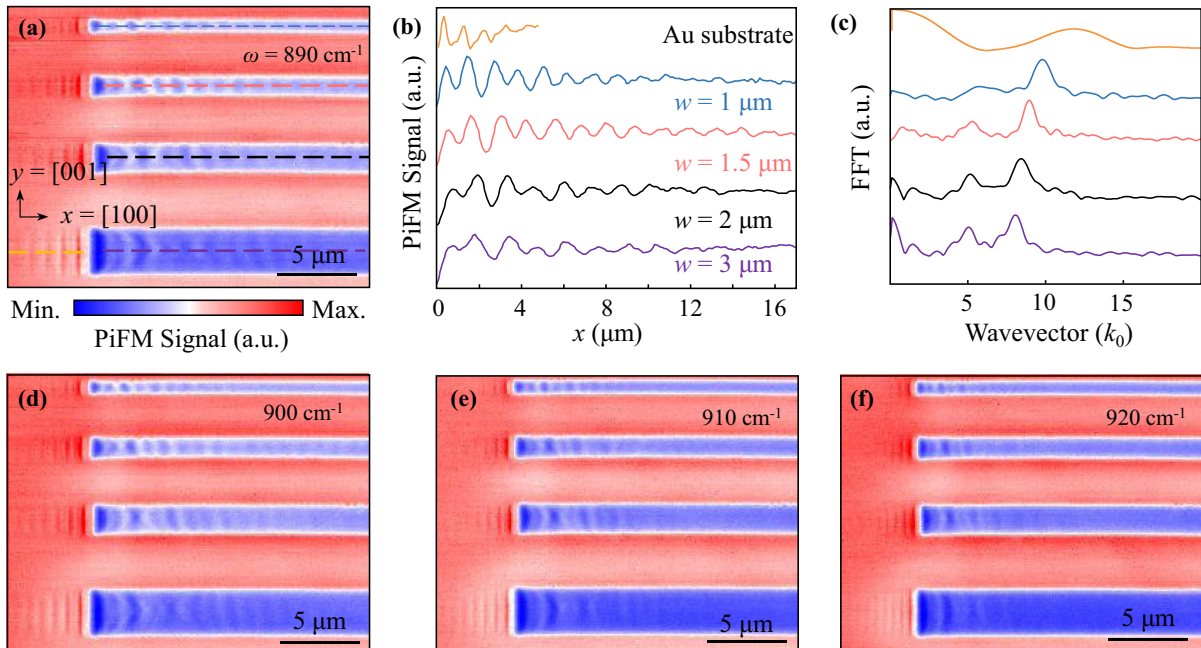


**Fig. 2.** Controlling the waveguide mode of HPhPs in  $\alpha$ -MoO<sub>3</sub> by varying the gold slit width. (a) Real space near-field nano-images of the waveguide mode of HPhPs with varying widths of gold slit. The frequency of the incident light is  $\omega = 890 \text{ cm}^{-1}$ . (b) PiFM signal amplitude fringe profiles extracted along the dashed lines in (a). (c) FFT on the near-field fringe profiles in (b). The abscissa is the incident light's wave vector ( $k_0 = 2\pi\omega$ ). (d)–(f) Near-field images recorded with three representative excitation frequencies. The thickness of  $\alpha$ -MoO<sub>3</sub> measured by AFM is 242 nm.

be achieved by controlling the waveguide width. Note that, with the increase of waveguide width, the proportion of sub-peak of FFT gradually increases, indicating that HPhPs contain two modes in the waveguide, which will be discussed in detail later. To further demonstrate the tunability of the HPhPs waveguide mode in a broad spectral range, the incident light with different wavenumbers between 900 and 920  $\text{cm}^{-1}$  is used to illuminate the sample [Figs. 2(d)–2(f)]. With the increase in frequency, the fringe period of HPhPs in the waveguide decreases gradually, and the loss increases gradually.

As the waveguide width is further reduced, it is found that the number of HPhPs fringes decreases sharply in the nanometer-scale ultranarrow waveguides. It is mainly attributed to the decrease of the excitation efficiency as the size of the excitation becomes much narrower in the nanometer-scale ultranarrow waveguides. We propose a solution to this issue by introducing an extended port at the waveguide port. As shown in Fig. 3(a), the HPhPs excited in the 220 nm ultranarrow waveguide with an extended port exhibit a more pronounced amplitude compared to that without an extended port. This indicates that the extended port effectively stimulates the propagation of HPhPs in the ultranarrow  $\alpha$ - $\text{MoO}_3$  waveguide. Interestingly, in Fig. 3(a), it is shown that the wavelength of HPhPs excited by the waveguide with an extended port is twice that of the waveguide without an extended port. This derives from the two contributions in the experimental setup.

(1) The direct contribution, in which guided modes launched by the waveguide port propagate until they reach the tip. For guided modes, this contribution appears as fringes

with periodicity approximately equal to the polariton wavelength,  $\lambda_p$ .

(2) The round-trip contribution, in which the guided mode is excited by the tip, reflected by the waveguide port, and reaches back to the tip. This contribution also appears as fringes for guided modes, but the periodicity is half of  $\lambda_p$ . This is because polaritons propagate twice between the tip and the waveguide port. This also explains the presence of two peaks in the FFT shown in Fig. 2(c). Therefore, the gradual increase of waveguide width leads to an increase of the direct contribution, as the wider waveguide port can excite more HPhPs, which explains the observed gradual increase in the subpeak of FFT in Fig. 2(c). On the other hand, the addition of an extended port to the waveguide port significantly increases the direct contribution while reducing the round-trip contribution, resulting in the predominant propagation of polaritons in the waveguide as  $\lambda_p$ . Figure 3(b) is the normalized fringe profiles in the waveguide of Fig. 3(a), which shows a more pronounced HPhPs amplitude in the waveguide with an extended port. This intuitively demonstrates the significantly improved polaritons excitation efficiency achievable with the extended port. Representative nanoimaging data are displayed in Figs. 3(c) and 3(d), where the wavenumbers of incident light are 900 and 910  $\text{cm}^{-1}$ , respectively. It is found that, although the polaritons loss increases with the increase of the incident light's wavenumber, the influence of the extended port of the waveguide is robust.

To quantitatively explain the impact of the extended port, the contrast of HPhPs fringe profiles in the waveguide composite structure can be defined as  $\text{contrast} = \frac{\tilde{E}_p - \tilde{E}_v}{\tilde{E}_p + \tilde{E}_v}$ , where

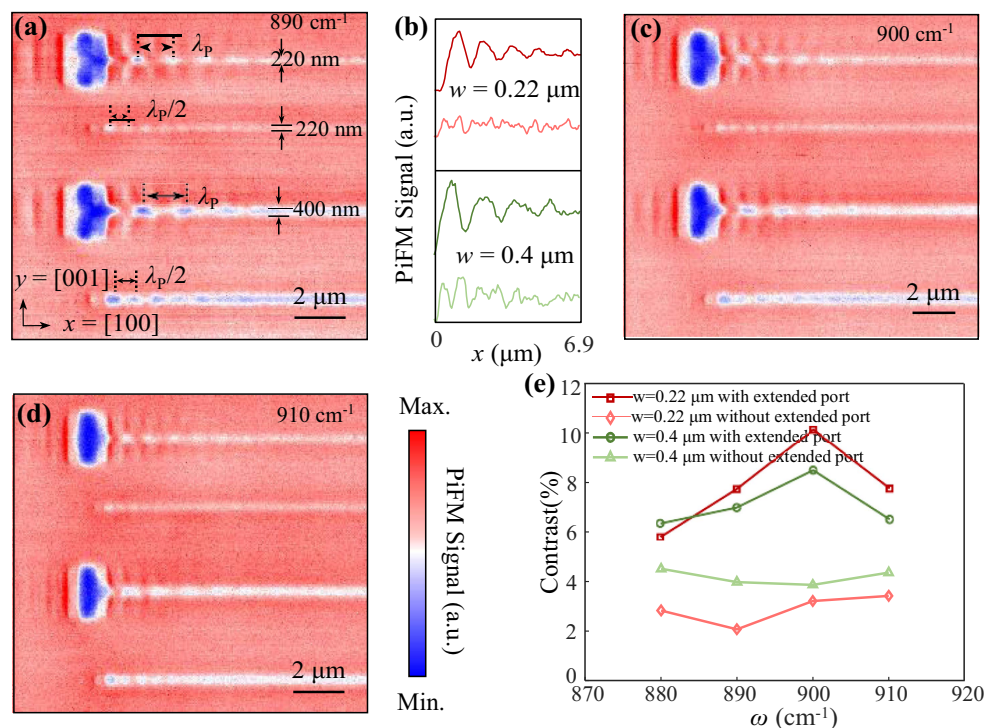


**Fig. 3.** Near-field manipulation of nanoscale ultra-narrow waveguides. (a) Near-field imaging of nanoscale waveguides with and without extended ports. (b) PiFM signal amplitude fringe profiles extracted along the center of waveguides in (a). (c), (d) Near-field images recorded with two representative excitation frequencies. (e) Comparison of the contrast of waveguides with and without extended ports. The geometry of all the extended ports is  $2 \mu\text{m} \times 1 \mu\text{m}$ . The thickness of  $\alpha$ - $\text{MoO}_3$  is 242 nm.

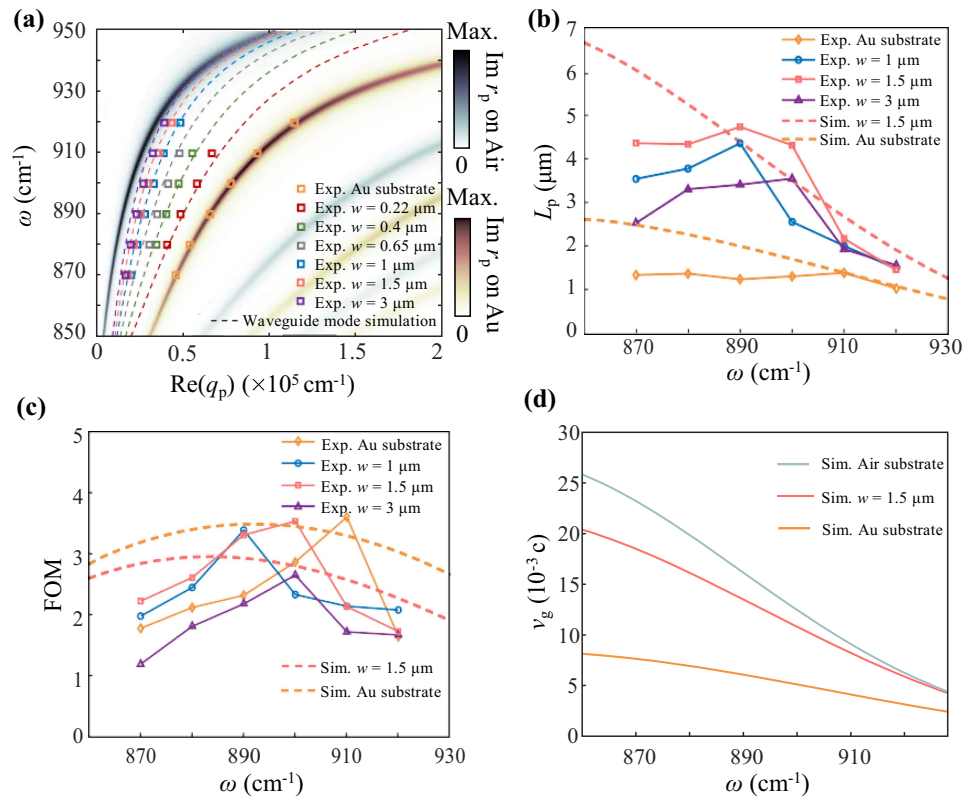


**Fig. 4.** Dispersion, propagation length, FOM, and  $v_g$  of the waveguide mode of HPhPs. (a) Dispersion relation of HPhPs in the  $\alpha$ -MoO<sub>3</sub> flake/gold slit composite structure. Colored squares indicate the experimental results obtained from PiFM images. Dashed colored lines correspond to the analytical dispersion relation of different waveguide widths. Pseudo-colored images represent the calculated  $\text{Im } r_p$  of the air/ $\alpha$ -MoO<sub>3</sub>/air or gold structure. (b) Theoretical (dashed colored lines) and experimental (colored marks) results of propagation length of HPhPs on different-width waveguide and gold substrate. (c) Theoretical (dashed colored lines) and experimental (colored marks) results of FOM of HPhPs on different-width waveguide and gold substrate. (d) Theoretical curves of group velocity of HPhPs on air substrate, 1.5  $\mu\text{m}$  waveguide, and gold substrate.

$\bar{E}_p$  and  $\bar{E}_v$  are the averaged peak and valley values of the fringe, respectively. The higher the contrast, the amplitude fluctuation of the fringes will be greater. Therefore, the magnitude of the contrast can also be understood as the excitation efficiency of HPhPs. Figure 3(e) lists the obtained values of the contrast from our experimental results on 0.22 and 0.4  $\mu\text{m}$  waveguides (see calculation process in Appendix C). The result indicates that the 0.22  $\mu\text{m}$  waveguide with an extended port has a contrast approximately three times larger than that of the waveguide without an extended port. As the  $w$  increases, the effectiveness of the extended port decreases, which is understandable since a wider waveguide can already excite sufficient HPhPs without additional compensation (Fig. 8 in the Appendix C). We predict that this method is suitable for narrower waveguides, and the benefit of the extended port will be further improved.

Although precise tuning of HPhPs has been experimentally achieved, the predictive computation of the HPhPs waveguide wave vectors is essential for the development of more advanced applications. Therefore, here we use a false-color plot of  $\text{Im } r_p$  to show the dispersion relation of  $\alpha$ -MoO<sub>3</sub> on air and gold substrate in Fig. 4(a) (see Appendix B). The waveguide dispersion relation [dashed lines in Fig. 4(a)] of different  $w$  is calculated by 2D simulations of the waveguide cross-section (see Section 5).

The experimental data points obtained from the FFT of the waveguide fringe profiles are in excellent agreement with the numerical simulation results. The wave vector in the waveguide exhibits a huge tuning range between the dispersion curve of  $\alpha$ -MoO<sub>3</sub> on the air substrate and the gold substrate. In detail, the compression ratio of HPhPs wavelength relative to the incident light wavelength, ranging from 8.6% to 35%, can be tuned by controlling the widths of the gold slit and the frequency of the incident light. We not only achieve a wide range modulation of HPhPs wavelength between the dispersions of  $\alpha$ -MoO<sub>3</sub> on air substrate and gold substrate but also obtain a high compression ratio. Typically, conventional dielectric substrates (such as silicon dioxide) can only achieve compression ratios of approximately 16.6% (the data were obtained through theoretical calculation on  $\alpha$ -MoO<sub>3</sub> at 242 nm and 910 cm<sup>-1</sup>). Compared with current complex methods for manipulating phonons (such as hexagonal boron nitride metasurface, heterostructures of twisted  $\alpha$ -MoO<sub>3</sub> crystal flakes, or the hybridized system), we demonstrate a high-quality HPhPs manipulation method using the  $\alpha$ -MoO<sub>3</sub> flake/gold slit composite structure. The fabrication process of the composite structure has no damage to the surface of  $\alpha$ -MoO<sub>3</sub>, and the waveguide is in a suspended state, which minimizes the source of HPhPs loss. Furthermore, the waveguide we designed is in the same plane,

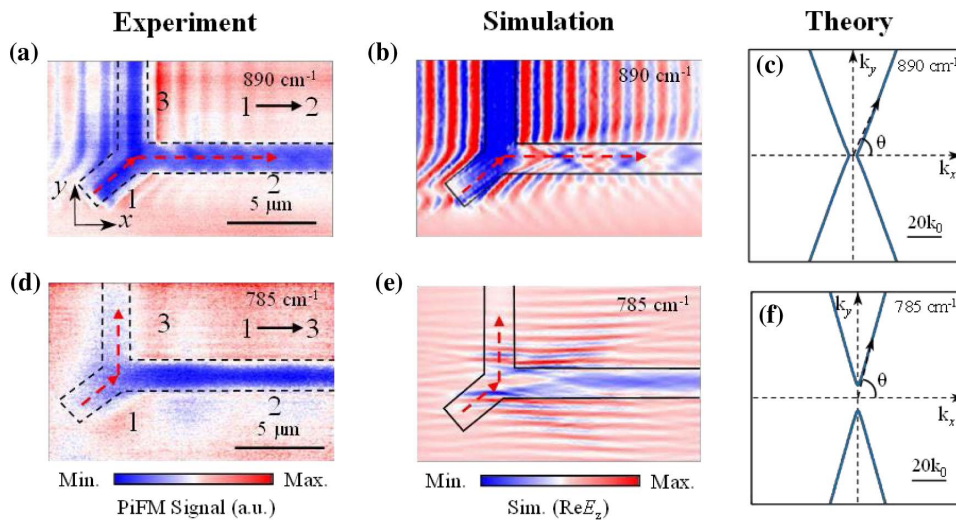


**Fig. 5.** Real-space visualization of Y-shaped routing waveguide. (a) Experimental near-field images of HPhPs propagating in a 305 nm thick  $\alpha$ -MoO<sub>3</sub> flake on a Y-shaped gold slit at  $\omega = 890$  cm<sup>-1</sup>. (b) Simulation result using the same parameters as those in (a). The red dashed arrows in (a) and (b) represent the waveguide's energy flow direction. (c) Analytic IFC of  $\alpha$ -MoO<sub>3</sub>/air at  $\omega = 890$  cm<sup>-1</sup>. (d) Experimental near-field images of HPhPs propagating in a 305 nm thick  $\alpha$ -MoO<sub>3</sub> flake on a Y-shaped gold slit at  $\omega = 785$  cm<sup>-1</sup>. (e) Simulation results using the same parameters as those in (d). The red dashed arrows in (d) and (e) represent the waveguide's energy flow direction. (f) Analytic IFC of  $\alpha$ -MoO<sub>3</sub>/air at  $\omega = 785$  cm<sup>-1</sup>.

which makes it compatible and stable, and provides a good platform for designing nanophotonic devices.

In addition, the propagation length ( $L_p$ ), figure of merit (FOM), and group velocity ( $v_g$ ) of HPhPs in the waveguide can be calculated by measuring the line widths of the FFT peaks (see Section 5). The obtained  $L_p$ , plotted in Fig. 4(b), decreases roughly as the incident light wavenumber increases. The obtained FOM, plotted in Fig. 4(c), increases first and then decreases as the incident light wavenumber increases. In Fig. 4(d), it is observed that  $v_g$  in the composite structure is decreased as the incident light frequency increases, resulting in a reduced propagation distance of HPhPs. The simulation curve [dashed lines in Figs. 4(b) and 4(c)] is calculated by 2D simulations of the waveguide cross-section (see Section 5). We can find that the theoretical curve and experimental data trends are consistent but not in complete agreement, which can be attributed to multiple factors: (i) the 2D cross-sectional simulation assumes that all the light entering the waveguide from the port is directed into the waveguide, whereas in reality, the effect of the waveguide width on the HPhPs needs to be considered; and (ii) in the experiment, when the waveguide width is sufficiently wide, the HPhPs propagate in a hyperbolic manner, resulting in less energy concentration and faster dissipation. The energy of HPhPs excited on the surface of  $\alpha$ -MoO<sub>3</sub> propagates in the form of divergence. As the waveguide width decreases, its divergence surface is localized to a certain extent, and its energy can be kept more concentrated, resulting in a longer propagation distance. However, when the width continues to decrease, the reduction in HPhPs excitation at the waveguide port leads to a decrease in propagation distance. This is because a more intense resonant source is a better launcher for polaritons, resulting in longer propagation distances. However, the propagation decay (i.e., FOM) is independent of the excitation source,

as it is an intrinsic property. In our experimental system,  $w = 1.5$   $\mu\text{m}$  is optimal, where  $L_p$  reaches 4.7  $\mu\text{m}$  and FOM reaches 3.5. Notably, the suspended  $\alpha$ -MoO<sub>3</sub> was reported by Shen *et al.* [45], where  $L_p = 2.0$   $\mu\text{m}$  and FOM = 3.2. Since the gold film in our experiment is obtained through electron beam evaporation, we believe that using monocrystalline gold can achieve atomic-level surface roughness, thereby reducing phonon losses at the waveguide boundaries and further increasing FOM. Furthermore, the thickness of the  $\alpha$ -MoO<sub>3</sub> layer we utilized is 242 nm. Theoretically, however, the selection of  $\alpha$ -MoO<sub>3</sub> flake thickness is unrestricted. However, in near-field experiments, as the thickness decreases, the light confinement capability of the flake diminishes gradually, while the detectable evanescent waves of HPhPs in  $\alpha$ -MoO<sub>3</sub> flake gradually increase. In the experiment, it is appropriate to choose an  $\alpha$ -MoO<sub>3</sub> thickness of approximately 300 nm.

In on-chip photonics, controlling the direction of energy flow at the nanoscale has profound implications for fundamental research on routing, energy management, and harvesting. Here, we design a Y-shaped waveguide composite structure to demonstrate that our system can support such behavior [see the optical image in Fig. 10(a), Appendix D]. As shown in the near-field nanoimaging of Fig. 5(a), we observe that, at 890 cm<sup>-1</sup> (in RB2), the polaritons in the waveguide propagate from Channel 1 to Channel 2, while propagation in Channel 3 is forbidden. The unique directional selectivity derives from the in-plane anisotropy of  $\alpha$ -MoO<sub>3</sub>, which demonstrates angle-dependent selectivity [Figs. 10(b) and 10(c), Appendix D]. It is worth noting that the diameter of the focal spot of the mid-infrared incident light (785–920 cm<sup>-1</sup>) is about 20  $\mu\text{m}$  so that the entire Y-shaped waveguide is illuminated. Meanwhile, PiFM involves tip scanning on the sample, indicating that each

pixel on the PiFM image is excited by the incident light. Therefore, HPhPs can be excited at the port, the sidewalls as well as the corner of a Y-shaped waveguide. Since the sidewall-excited HPhPs cannot be well coupled into the waveguide, so the sidewall-excited HPhPs will leak some energy. Figure 5(c) illustrates the theory of how the waveguide orientation angle affects the propagation of polaritons. The polaritons can only be excited when the angle of the waveguide wave vector is within the open angle of the hyperbolic IFC, i.e.,  $\theta < \theta_{\text{open}} = \arctan(\sqrt{-\epsilon_x}/\sqrt{-\epsilon_y})$ . Consequently, these polaritons can be strictly confined within Channels 1 and 2 and are in good agreement with numerical simulation mimicking the experiment [Fig. 5(b)]. When the incident light wavenumber is changed to  $785 \text{ cm}^{-1}$  (in RB1), Channel 2 is forbidden, and polaritons propagate from Channel 1 to Channel 3 [Fig. 5(d)]. The corresponding simulation in Fig. 5(e) also demonstrates this well. The results indicate that we have successfully realized an infrared routing device in a Y-shaped waveguide structure. It is worth noting that, in RB1, the open angle direction of the IFC has changed [Fig. 5(f)] so that  $\theta_{\text{open}} < \theta < 90^\circ$ . In the Y-shaped waveguide structure we designed, Channel 1 is designed to have an angle of  $40^\circ$  with the  $x$  axis, which is less than  $\theta_{\text{open}}$  at  $785 \text{ cm}^{-1}$ . However, experiment and simulation results observe polaritons in Channel 1 and Channel 3, because the sidewalls of the waveguide can also excite polaritons that satisfy the conditions. To enable phonon polariton excitation at the port of Channel 1, future work may involve searching for light sources with lower wavenumbers. Furthermore, another way to achieve routing may be through various compensatory methods, such as control over carrier density using graphene doping or employing electrical gating.

#### 4. CONCLUSION

In summary, we propose a new composite structure of planar waveguide device in the midinfrared range that is using highly oriented HPhPs in  $\alpha\text{-MoO}_3$ , launched by gold slits with different widths. By changing the waveguide width and combining them with theoretical dispersion curves, the compression ratio of HPhPs wavelength relative to the incident light wavelength can be precisely tuned from 35% to 8.6%. In particular, we realized the excitation of HPhPs in nanoscale waveguides by adding an extended port to the waveguide port. By analyzing the internal loss of the waveguide, the optimal waveguide width is identified for exciting HPhPs. Furthermore, we designed a Y-shaped waveguide, realizing the routing of HPhPs. In addition, by selecting other anisotropic van der Waals (vdW) materials, we anticipate that the concept of this composite structure will apply to the midinfrared to terahertz regime. Our work provides a convenient and robust method to effectively manipulate the propagation and routing characteristics of phonon polaritons in natural vdW materials, which will advance on-chip photonics research.

#### 5. METHODS

##### A. Sample Preparations

A 100 nm thick gold film with a 5 nm thick Cr adhesion layer was deposited on a standard Si wafer with a 300 nm thick  $\text{SiO}_2$  layer substrate using electron beam evaporation. The slits of

different widths in the gold substrate were made by focused ion beam (FIB) lithography in an FEI Helios NanoLab G3 dual-beam FIB-SEM system. Note that a 0.1 nA etching current was used for slits with a width below 500 nm, while a 0.3 nA etching current was used for the rest to maintain the aspect ratio of the slits consistent with the design. Our  $\alpha\text{-MoO}_3$  flakes were exfoliated from a bulk crystal (purchased from SixCarbon Technology) using a polydimethylsiloxane (PDMS) sheet. First, by using a microscope, we selected a large, homogeneous, and ultrathin flake that was sufficient to cover the entire pattern on the substrate and then transferred it onto the structure of the substrate.

##### B. PiFM Measurements

A VistaScope microscope from Molecular Vista Inc. was used for the PiFM measurements. The microscope was coupled to a Laser Tune quantum cascade laser (QCL) system from Block Engineering with a tuning range from  $780$  to  $1900 \text{ cm}^{-1}$  and a wave number resolution of  $0.5 \text{ cm}^{-1}$ . The sample was side-illuminated with the 30 ns pulsed beam and an adjustable repetition rate at the  $38^\circ$  angle from the sample surface by a parabolic mirror with a numerical aperture of around 0.4. The excitation laser was focused by the parabolic mirror to an elliptical spot with a size of  $2\lambda$  and  $2.5\lambda$  ( $\lambda$  is the wavelength of the incident light) for the short axis and long axis, respectively. An average laser power of 1.5 mW was used at the sample surface. The microscope was operated in tapping mode with a gold-coated Si cantilever obtained from NCH-Au noncontact cantilevers from Nanosensors. The pulsed QCL beam was modulated by tuning its repetition rate to the difference frequency of the cantilever's eigenmodes at  $f_m = f_1 - f_0$  (referred to as sideband modulation mode), where  $f_0$  and  $f_1$  are the first- and second-order resonance frequencies of the AFM cantilever, respectively. The second eigenmode was used for tip-sample distance stabilization, with a tapping modulation amplitude of a few nanometers and a typical setpoint of between 70% and 80%. The first eigenmode of the AFM cantilever was used for PiFM detection; the second eigenmode was used for the AFM topography of the sample. The incident light was always oriented along the  $x$  axis of the  $\alpha\text{-MoO}_3$  flake during all the measurements.

##### C. Numerical Simulations

In this study, we simulated PiFM near-field images using the finite-element-method numerical software COMSOL Multiphysics. A 2D cross-sectional structure of  $\alpha\text{-MoO}_3$  placed on a gold substrate and an air substrate is simulated in Fig. 1(b). The dipole polarized along the  $z$  direction was placed 100 nm away from the surface of  $\alpha\text{-MoO}_3$  to excite HPhPs [Figs. 1(b), 1(e), and 1(f)]. For 3D simulations, the whole system was illuminated with plane waves with linear polarization along the  $x$  axis [Figs. 1(c), 1(d), and 5(b)] and linear polarization along the  $y$  axis [Fig. 5(e)], respectively. The real part of the vertical component of the electric field  $\text{Re}(E_z)$  was collected from 20 nm above the  $\alpha\text{-MoO}_3$  surface to obtain the near-field images. Meshing types and sizes were optimized to ensure good convergence of simulated results. Furthermore, the dispersion relation of the waveguides was calculated via 2D simulations of their cross-sections, done in Mode Solutions (the dashed lines

in Fig. 4; see Appendix E for more details). The permittivity of  $\alpha$ -MoO<sub>3</sub> was described by using the Lorentz model (details are presented in Appendix A), while the dielectric constants of gold were obtained from the database in COMSOL. To minimize the artificial oscillations in the output FFT profiles, apodization was performed by using the Hanning windowing function. In addition, to increase the resolving power of FFT, zero-filling/padding was done by extending the interferogram by a factor of 100 by adding zeros.

#### D. Calculation of the Propagation Length and Figure of Merit of Hyperbolic Phonon Polaritons

By positioning the FFT peak of the near-field waveguide fringe profiles and measuring its linewidth, we obtained the full complex-valued wave vector,  $q_p = q'_p + iq''_p$ . Therefore, we obtain the propagation length  $L_p = 1/q''_p$ , the figure of merit  $\text{FOM} = q'_p/q''_p$ , and the group velocity  $v_g = \frac{\partial \omega}{\partial q_p}$ .

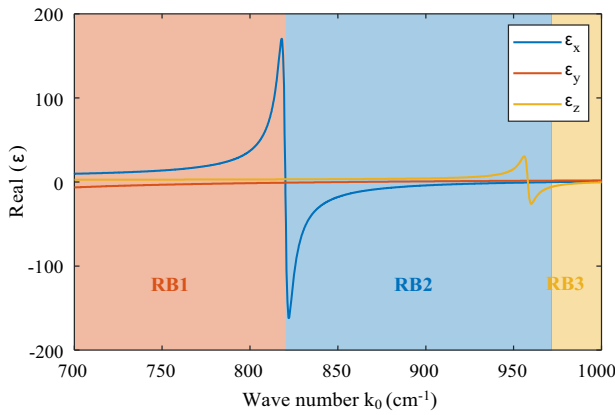


**Fig. 6.** Real-part permittivities of  $\alpha$ -MoO<sub>3</sub>, where three different Reststrahlen bands of  $\alpha$ -MoO<sub>3</sub> are shaded in different colors.

**Table 1.** Parameters Used for Calculating the Permittivities of  $\alpha$ -MoO<sub>3</sub> [39]

Direction	$x$	$y$	$z$
$\epsilon_\infty$	4	5.2	2.4
$\omega_{\text{LO}}$ (cm <sup>-1</sup> )	972	851	1004
$\omega_{\text{TO}}$ (cm <sup>-1</sup> )	820	545	958
$\gamma$ (cm <sup>-1</sup> )	4	4	2

#### APPENDIX A: DIELECTRIC FUNCTION OF $\alpha$ -MoO<sub>3</sub>

As shown in Fig. 6, in the midinfrared region, the optical response of  $\alpha$ -MoO<sub>3</sub> is mainly phonon absorption, and the dielectric function can be described by the Lorentz equation [4]:

$$\epsilon_j(\omega) = \epsilon_\alpha^j \left( 1 + \frac{\omega_{\text{LO}}^j{}^2 - \omega_{\text{TO}}^j{}^2}{\omega_{\text{TO}}^j{}^2 - \omega^2 - i\omega\gamma^j} \right), \quad j = x, y, z, \quad (\text{A1})$$

where  $\omega_{\text{LO}}$ ,  $\omega_{\text{TO}}$ ,  $\gamma$ , and  $\epsilon_\alpha$  are the LO and TO phonon frequencies, phonon damping, and the high-frequency permittivity, respectively. The fitting parameters are listed in Table 1. Figure 7 shows the characterization of  $\alpha$ -MoO<sub>3</sub> flake/gold slits composite structure, which indicates that the long axis of the waveguide is along the [100] crystal direction of  $\alpha$ -MoO<sub>3</sub>.

#### APPENDIX B: CALCULATIONS ON THE ISOFREQUENCY CURVES AND COMPLEX REFLECTIVITY OF $\alpha$ -MoO<sub>3</sub>

For the description of the isofrequency curves (IFCs) of  $\alpha$ -MoO<sub>3</sub>, it can be analytically calculated by recently derived formalism [39]:

$$q = \frac{\rho}{k_0 d} \left[ \arctan\left(\frac{\epsilon_1 \rho}{\epsilon_z}\right) + \arctan\left(\frac{\epsilon_3 \rho}{\epsilon_z}\right) + \pi l \right], \quad l = 0, 1, 2, \dots, \quad (\text{B1})$$

where  $q = \sqrt{\left(\frac{k_x}{k_0}\right)^2 + \left(\frac{k_y}{k_0}\right)^2}$  is the normalized in-plane wave vector, the parameter  $\rho = \sqrt{i \frac{\epsilon_z q^2}{\epsilon_x q_x^2 + \epsilon_y q_y^2}}$ ,  $d$  is the thickness of the  $\alpha$ -MoO<sub>3</sub> slab,  $\epsilon_1$  and  $\epsilon_3$  are the permittivities of the superstrate and substrate, respectively, and  $l$  is the order of TM modes.

The HPhPs dispersion relation of the  $\alpha$ -MoO<sub>3</sub> flake can be manifested by the complex reflectivity  $r_p(\omega, q)$  of a multi-layer structure consisting of air/ $\alpha$ -MoO<sub>3</sub>/substrate. The total reflectivity of this system is determined by the following equations [4]:

$$r_p = \frac{r_1 + r_3 e^{i2k_2 d}}{1 + r_1 r_3 e^{i2k_2 d}}, \quad (\text{B2})$$

$$r_1 = \frac{\epsilon_\perp k_1 - \epsilon_1 k_2}{\epsilon_\perp k_1 + \epsilon_1 k_2}, \quad (\text{B3})$$

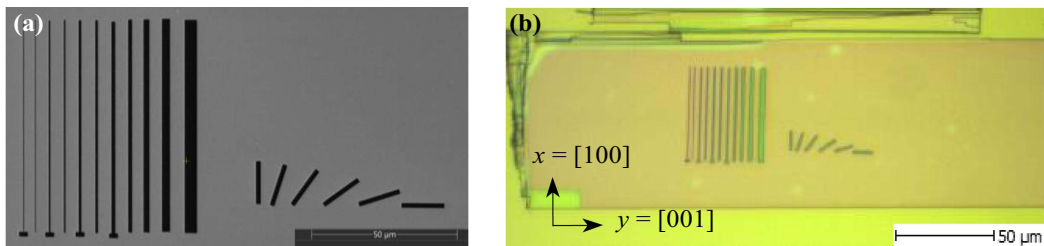
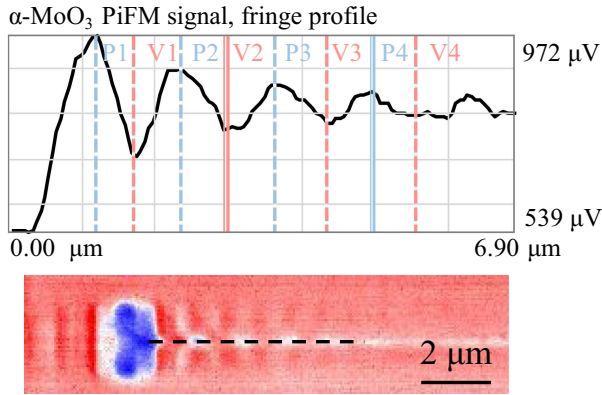


**Fig. 7.** Characterization of  $\alpha$ -MoO<sub>3</sub> flake/gold slits composite structure. (a) SEM image of gold slits. (b) Optical microscopy image of  $\alpha$ -MoO<sub>3</sub> flake/gold slits composite structure.

$$r_3 = \frac{\epsilon_3 k_2 - \epsilon_\perp k_3}{\epsilon_3 k_2 + \epsilon_\perp k_3}, \quad (\text{B4})$$

where the subscripts 1, 2, and 3 denote the air,  $\alpha\text{-MoO}_3$ , and the substrate, respectively. The parameters  $r_1$  and  $r_3$  delegate the reflectivities at the air/ $\alpha\text{-MoO}_3$  and  $\alpha\text{-MoO}_3$ /substrate interfaces, respectively. The  $\epsilon_j$  ( $j = 1, 3$ , and  $\perp$ ) refers to the relative permittivities of the air, substrate, and  $\epsilon_x$  (or  $\epsilon_y$ ). For  $j = 1$  and 3, the momenta are given by  $k_j = \sqrt{\epsilon_j(\frac{\omega}{c})^2 - q^2}$  and  $k_2 = \sqrt{\omega_\perp(\frac{\omega}{c})^2 - \frac{\epsilon_\perp}{\epsilon_\parallel} q^2}$ .



PiFM signal	1	2	3	4
Peak (blue) ( $\mu\text{V}$ )	967.9	895.4	864.5	843.7
Valley (red) ( $\mu\text{V}$ )	708.6	771.9	779.0	797.1

**Fig. 8.** Fringe profiles in the 220 nm waveguide with extended port at  $890\text{ cm}^{-1}$  [Fig. 3(a) in the main text].

### APPENDIX C: CALCULATION OF THE CONTRAST OF THE HPHPS FRINGES IN NEAR-FIELD IMAGES

In Fig. 8, we extract part of the 220 nm waveguide’s fringe profile in Fig. 3(a) as a demonstration to briefly describe the calculation process of the contrast. By extracting the central profile of the waveguide (black dotted line in Fig. 8), we can obtain the accurate value of the wave peak and valley. In the 220 nm waveguide with an extended port at  $890\text{ cm}^{-1}$ , the averaged peak value  $\bar{E}_p = 892.9\ \mu\text{V}$ , and the averaged valley value  $\bar{E}_v = 764.2\ \mu\text{V}$ . Hence, the contrast of HPhPs fringe profiles in the waveguide is given by contrast  $= \frac{\bar{E}_p - \bar{E}_v}{\bar{E}_p + \bar{E}_v} = 7.77\%$ .

### APPENDIX D: NEAR-FIELD IMAGES OF 650 nm AND 1 μm WAVEGUIDES WITH OR WITHOUT EXTENDED PORT

As shown in Fig. 9, with the increase of waveguide width, it is found that the benefit of the extended port band decreases continuously. This is understandable because, with a wide enough waveguide, its facets are already capable of exciting a large number of HPhPs into the waveguide without requiring additional compensation. Indeed, for a waveguide with enough width, the extended port not only fails to facilitate the excitation of more HPhPs into the waveguide but also increases the loss of HPhPs due to the additional increase in transmission distance introduced by the extended port.

Additionally, in Fig. 10, we design waveguide structures with a rotation angle and test their near-field images of HPhPs propagating in waveguides. The unique directional selectivity derives from the in-plane anisotropy of  $\alpha\text{-MoO}_3$ , which demonstrates angle-dependent selectivity.

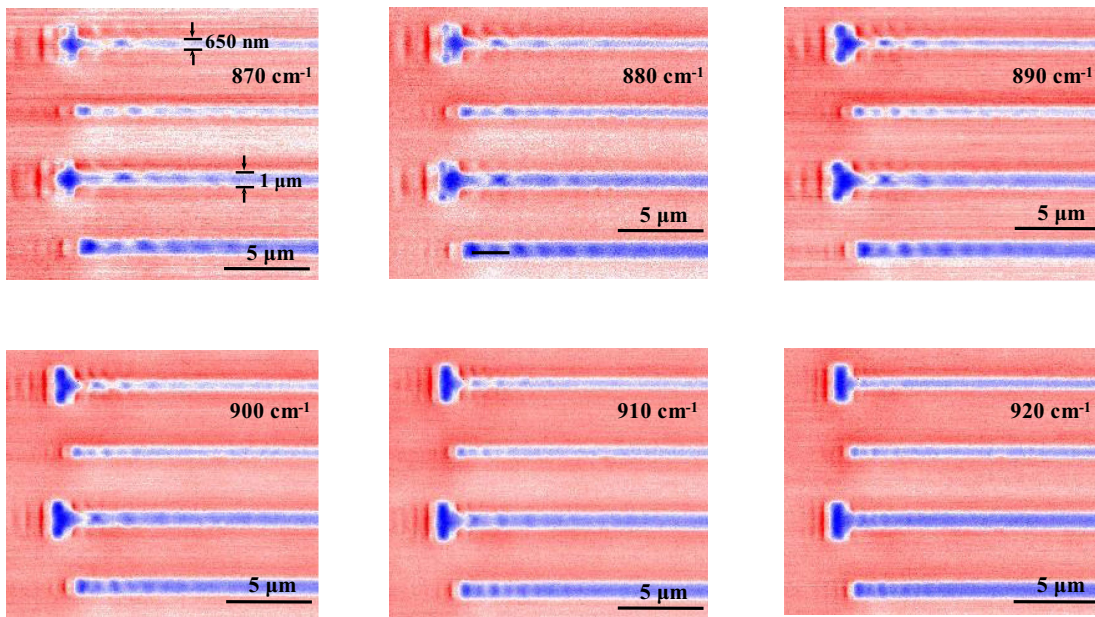


**Fig. 9.** Near-field images of 650 nm and 1  $\mu\text{m}$  waveguides at different frequencies.

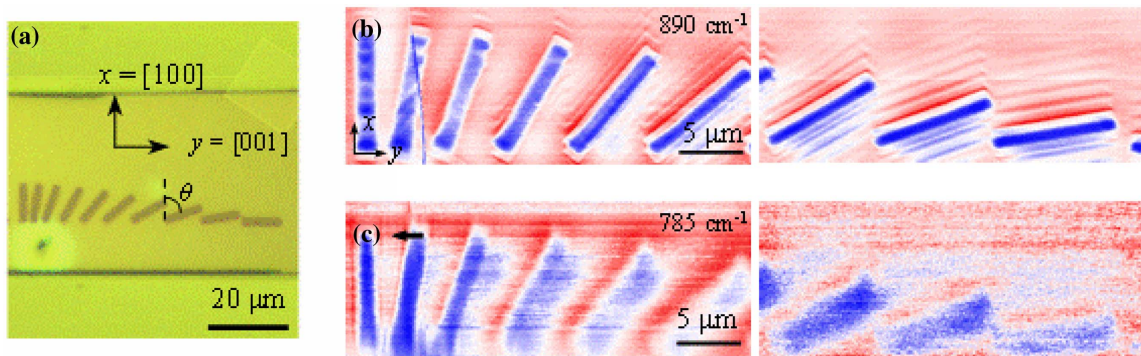


**Fig. 10.** (a) The optical microscopy image of waveguide structure with a rotation angle.  $\theta$  is the angle between the longitudinal axis of the waveguide and the  $x$  axis. The thickness of the  $\alpha$ - $\text{MoO}_3$  flake is 305 nm. (b) The experimental near-field images of HPhPs propagating in waveguides with different  $\theta$  (from left to right, the values of  $\theta$  are  $0^\circ$ ,  $10^\circ$ ,  $20^\circ$ ,  $30^\circ$ ,  $40^\circ$ ,  $50^\circ$ ,  $60^\circ$ ,  $70^\circ$ , and  $80^\circ$ ) at  $890\text{ cm}^{-1}$ . Due to the limitations of the scanning range in the near-field experiment, the figure was divided into two scans, referred to as the left image and the right image, respectively. (c) The same as (b) except that the excitation frequency of incident light is  $785\text{ cm}^{-1}$ .

## APPENDIX E: HPHS DISPERSION SIMULATION OF $\alpha$ - $\text{MoO}_3$ UNDER GOLD SLIT WAVEGUIDE

The dispersion relation (dashed lines) in Fig. 4(a) of the  $\alpha$ - $\text{MoO}_3$ /gold slit hybrid waveguide was calculated via 2D simulations of their cross-sections, done in Mode Solutions. For example, as shown in Fig. 11, when the slit width is  $1.5\text{ }\mu\text{m}$ ,

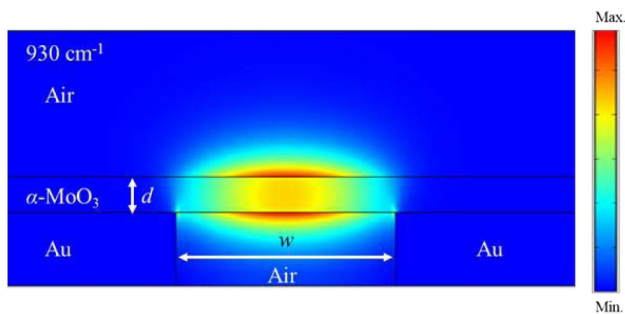


**Fig. 11.** 2D simulation of the electric field distribution in the cross-section of a waveguide with a slit width of  $1.5\text{ }\mu\text{m}$  at  $930\text{ cm}^{-1}$ .

the  $930\text{ cm}^{-1}$  is used to excite the 2D cross-section of the composite structure. It can be observed that the energy is well localized within the  $\alpha$ - $\text{MoO}_3$ /Au slit. Furthermore, through the simulation, we can obtain the effective permittivity of the composite structure waveguide at this width. By scanning the frequency of the incident light and the waveguide width, we can accurately obtain the dispersion relationship. As shown in Fig. 4(a), the experimental results are in good agreement with the simulation.

**Funding.** National Natural Science Foundation of China (12274157, 12021004, 12274334, 11904271); National Key Research and Development Program of China (2022YFA1604403); Natural Science Foundation of Hubei Province of China (2023AFA076).

**Acknowledgment.** Special thanks are given to the Analytical and Testing Center of HUST and the Center of Micro-Fabrication and Characterization (CMFC) of WNLO for the use of their facilities.

**Disclosures.** The authors declare no conflicts of interest.

**Data Availability.** Data underlying the results presented in this paper are not publicly available at this time but may be obtained from the authors upon reasonable request.

## REFERENCES

- S. Dai, Z. Fei, Q. Ma, *et al.*, "Tunable phonon polaritons in atomically thin van der Waals crystals of boron nitride," *Science* **343**, 1125–1129 (2014).
- L. Wang, N. J. Long, L. Li, *et al.*, "Multi-functional bismuth-doped bioglasses: combining bioactivity and photothermal response for bone tumor treatment and tissue repair," *Light Sci. Appl.* **7**, 1 (2018).
- W. Ma, P. Alonso-González, S. Li, *et al.*, "In-plane anisotropic and ultra-low-loss polaritons in a natural van der Waals crystal," *Nature* **562**, 557–562 (2018).
- Z. Zheng, N. Xu, S. L. Oscurato, *et al.*, "A mid-infrared biaxial hyperbolic van der Waals crystal," *Sci. Adv.* **5**, eaav8690 (2019).
- Z. Zheng, J. Chen, Y. Wang, *et al.*, "Highly confined and tunable hyperbolic phonon polaritons in van der Waals semiconducting transition metal oxides," *Adv. Mater.* **30**, 1705318 (2018).
- J. Taboada-Gutiérrez, G. Álvarez-Pérez, J. Duan, *et al.*, "Broad spectral tuning of ultra-low-loss polaritons in a van der Waals crystal by intercalation," *Nat. Mater.* **19**, 964–968 (2020).
- S. Dai, Q. Ma, T. Andersen, *et al.*, "Subdiffractive focusing and guiding of polaritonic rays in a natural hyperbolic material," *Nat. Commun.* **6**, 6963 (2015).
- E. Yoxall, M. Schnell, A. Y. Nikitin, *et al.*, "Direct observation of ultra-slow hyperbolic polariton propagation with negative phase velocity," *Nat. Photonics* **9**, 674–678 (2015).
- G. Hu, W. Ma, D. Hu, *et al.*, "Real-space nanoimaging of hyperbolic shear polaritons in a monoclinic crystal," *Nat. Nanotechnol.* **18**, 64–70 (2023).
- N. C. Passler, X. Ni, G. Hu, *et al.*, "Hyperbolic shear polaritons in low-symmetry crystals," *Nature* **602**, 595–600 (2022).
- I.-H. Lee, M. He, X. Zhang, *et al.*, "Image polaritons in boron nitride for extreme polariton confinement with low losses," *Nat. Commun.* **11**, 3649 (2020).

12. P. Li, I. Dolado, F. J. Alfaro-Mozaz, *et al.*, "Infrared hyperbolic meta-surface based on nanostructured van der Waals materials," *Science* **359**, 892–896 (2018).
13. P. Li, G. Hu, I. Dolado, *et al.*, "Collective near-field coupling and non-local phenomena in infrared-phononic metasurfaces for nano-light canalization," *Nat. Commun.* **11**, 3663 (2020).
14. J. Lu, T. Sang, C. Pian, *et al.*, "Tailoring intrinsic chiroptical responses via twisted bilayer  $\alpha$ -MoO<sub>3</sub> separated by a VO<sub>2</sub> film," *APL Photonics* **9**, 046112 (2024).
15. Z. Zhou, R. Song, J. Xu, *et al.*, "Gate-tuning hybrid polaritons in twisted  $\alpha$ -MoO<sub>3</sub>/graphene heterostructures," *Nano Lett.* **23**, 11252–11259 (2023).
16. C. Pian, T. Sang, X. Zhang, *et al.*, "Hyperbolic phonon polaritons-induced photonic spin Hall effect in an  $\alpha$ -MoO<sub>3</sub> thin film," *Appl. Phys. Lett.* **124**, 121602 (2024).
17. K.-J. Tielrooij, N. C. H. Hesp, A. Principi, *et al.*, "Out-of-plane heat transfer in van der Waals stacks through electron–hyperbolic phonon coupling," *Nat. Nanotechnol.* **13**, 41–46 (2018).
18. M. Autore, P. Li, I. Dolado, *et al.*, "Boron nitride nanoresonators for phonon-enhanced molecular vibrational spectroscopy at the strong coupling limit," *Light Sci. Appl.* **7**, 17172 (2018).
19. A. Bylinkin, M. Schnell, M. Autore, *et al.*, "Real-space observation of vibrational strong coupling between propagating phonon polaritons and organic molecules," *Nat. Photonics* **15**, 197–202 (2021).
20. C. Sayrin, C. Junge, R. Mitsch, *et al.*, "Nanophotonic optical isolator controlled by the internal state of cold atoms," *Phys. Rev. X* **5**, 041036 (2015).
21. S. Castilla, I. Vangelidis, V.-V. Pusapati, *et al.*, "Plasmonic antenna coupling to hyperbolic phonon-polaritons for sensitive and fast mid-infrared photodetection with graphene," *Nat. Commun.* **11**, 4872 (2020).
22. W. Huang, F. Sun, Z. Zheng, *et al.*, "van der Waals phonon polariton microstructures for configurable infrared electromagnetic field localizations," *Adv. Sci.* **8**, 2170076 (2021).
23. I. D. Barcelos, T. A. Canassa, R. A. Mayer, *et al.*, "Ultrabroadband nanocavity of hyperbolic phonon–polaritons in 1D-like  $\alpha$ -MoO<sub>3</sub>," *ACS Photonics* **8**, 3017–3026 (2021).
24. S.-J. Yu, Y. Jiang, J. A. Roberts, *et al.*, "Ultrahigh-quality infrared polaritonic resonators based on bottom-up-synthesized van der Waals nanoribbons," *ACS Nano* **16**, 3027–3035 (2022).
25. M. Ye, B. Qiang, S. Zhu, *et al.*, "Nano-optical engineering of anisotropic phonon resonances in a hyperbolic  $\alpha$ -MoO<sub>3</sub> metamaterial," *Adv. Opt. Mater.* **10**, 2102096 (2022).
26. J. Yang, J. Tang, M. B. Ghasemian, *et al.*, "High-Q phonon-polaritons in spatially confined freestanding  $\alpha$ -MoO<sub>3</sub>," *ACS Photonics* **9**, 905–913 (2022).
27. Z. Dai, G. Hu, G. Si, *et al.*, "Edge-oriented and steerable hyperbolic polaritons in anisotropic van der Waals nanocavities," *Nat. Commun.* **11**, 6086 (2020).
28. J. Duan, G. Álvarez-Pérez, K. V. Voronin, *et al.*, "Enabling propagation of anisotropic polaritons along forbidden directions via a topological transition," *Sci. Adv.* **7**, eabf2690 (2021).
29. C. Hu, T. Sun, Y. Zeng, *et al.*, "Source-configured symmetry-broken hyperbolic polaritons," *eLight* **3**, 14 (2023).
30. A. Nemilentsau, T. Stauber, G. Gómez-Santos, *et al.*, "Switchable and unidirectional plasmonic beacons in hyperbolic two-dimensional materials," *Phys. Rev. B* **99**, 201405 (2019).
31. M. Chen, X. Lin, T. H. Dinh, *et al.*, "Configurable phonon polaritons in twisted  $\alpha$ -MoO<sub>3</sub>," *Nat. Mater.* **19**, 1307–1311 (2020).
32. Z. Zheng, F. Sun, W. Huang, *et al.*, "Phonon polaritons in twisted double-layers of hyperbolic van der Waals crystals," *Nano Lett.* **20**, 5301–5308 (2020).
33. G. Hu, Q. Ou, G. Si, *et al.*, "Topological polaritons and photonic magic angles in twisted  $\alpha$ -MoO<sub>3</sub> bilayers," *Nature* **582**, 209–213 (2020).
34. J. Duan, N. Capote-Robayna, J. Taboada-Gutiérrez, *et al.*, "Twisted nano-optics: manipulating light at the nanoscale with twisted phonon polaritonic slabs," *Nano Lett.* **20**, 5323–5329 (2020).
35. H. Hu, N. Chen, H. Teng, *et al.*, "Gate-tunable negative refraction of mid-infrared polaritons," *Science* **379**, 558–561 (2023).
36. X. Zhang, Q. Yan, W. Ma, *et al.*, "Ultrafast anisotropic dynamics of hyperbolic nanolight pulse propagation," *Sci. Adv.* **9**, eadi4407 (2023).
37. G. Lu, Z. Pan, C. R. Gubbin, *et al.*, "Launching and manipulation of higher-order in-plane hyperbolic phonon polaritons in low-dimensional heterostructures," *Adv. Mater.* **35**, 2300301 (2023).
38. J. Duan, R. Chen, J. Li, *et al.*, "Launching phonon polaritons by natural boron nitride wrinkles with modifiable dispersion by dielectric environments," *Adv. Mater.* **29**, 1702494 (2017).
39. Y. Qu, N. Chen, H. Teng, *et al.*, "Tunable planar focusing based on hyperbolic phonon polaritons in  $\alpha$ -MoO<sub>3</sub>," *Adv. Mater.* **34**, 2105590 (2022).
40. K. Chaudhary, M. Tamagnone, X. Yin, *et al.*, "Polariton nanophotonics using phase-change materials," *Nat. Commun.* **10**, 4487 (2019).
41. T. G. Folland, A. Fali, S. T. White, *et al.*, "Reconfigurable infrared hyperbolic metasurfaces using phase change materials," *Nat. Commun.* **9**, 4371 (2018).
42. J. Duan, G. Álvarez-Pérez, A. I. F. Tresguerres-Mata, *et al.*, "Planar refraction and lensing of highly confined polaritons in anisotropic media," *Nat. Commun.* **12**, 4325 (2021).
43. S. G. Menabde, J. Jahng, S. Boroviks, *et al.*, "Low-loss anisotropic image polaritons in van der Waals crystal  $\alpha$ -MoO<sub>3</sub>," *Adv. Opt. Mater.* **10**, 2201492 (2022).
44. Z. Zheng, F. Sun, N. Xu, *et al.*, "Tunable hyperbolic phonon polaritons in a suspended van der Waals  $\alpha$ -MoO<sub>3</sub> with gradient gaps," *Adv. Opt. Mater.* **10**, 2102057 (2022).
45. J. Shen, Z. Zheng, T. Dinh, *et al.*, "Hyperbolic phonon polaritons with positive and negative phase velocities in suspended  $\alpha$ -MoO<sub>3</sub>," *Appl. Phys. Lett.* **14**, 113101 (2022).
46. D. Nowak, W. Morrison, H. K. Wickramasinghe, *et al.*, "Nanoscale chemical imaging by photoinduced force microscopy," *Sci. Adv.* **2**, e1501571 (2016).
47. S. G. Menabde, J. T. Heiden, J. D. Cox, *et al.*, "Image polaritons in van der Waals crystals," *Nanophotonics* **11**, 2433–2452 (2022).